Meshfree simulations of injection molding processes

Lennart Veltmaat,[1] Felix Mehrens,[2] Hans-Josef Endres,[2] Jörg Kuhnert,[3] and Pratik Suchde[4]

[1)]*Volkswagen AG, Brieffach 011/1564/7, 38436 Wolfsburg, Germany*[a)]

[2)]*Institute of Plastics and Circular Economy, Leibniz University Hannover, An der Universität 2, 30823 Garbsen, Germany*

[3)]*Fraunhofer Institute of Industrial Mathematics, Fraunhofer-Platz 1, 67663 Kaiserslautern, Germany*

[4)]*University of Luxembourg, 2 avenue de l'université, L-4365 Esch-sur-alzette, Luxembourg*[b)]

(Dated: 24 February 2022)

In this paper, we introduce a meshfree numerical framework using the Finite Pointset Method (FPM) for the modeling and simulating of injection molding processes. When compared to well established mesh based methods which have been widely applied for these applications, our approach avoids the need to extensive pre-processing, and enables accurate treatment of free surfaces and other associated phenomena. To accurately model the polymer injections, we consider a detailed material model, with temperature dependent viscosity and density, while also considering shear thinning behavior with a strain rate dependent viscosity. Our numerical investigations show that injection molding-specific problems such as the modeling of viscous flows and the fountain flow effect can be successfully implemented using our presented framework. For a thorough validation of our proposed model, we compare the simulated flow behavior with injection molding experiments which are also performed in this work. The experimental setup considers the injection of a polymer melt into a spiral mold. The flow behavior is investigated experimentally at varying melt injection and wall temperature, with different threshold pressures. Our numerical simulations show a good comparison with these experimental results, both qualitatively and quantitatively. We also introduce a correction mechanism to ensure energy conservation, which has often been challenging in meshfree approaches. This work is the first time that the flow behavior in a mesh free injection molding method has been experimentally validated and successfully applied to the simulation of an actual industrial vehicle component.

[a)]Corresponding Author: lennart.veltmaat@volkswagen.de

[b)]Also at Fraunhofer Institute of Industrial Mathematics, Kaiserslautern, Germany

I. INTRODUCTION

The simulation of injection molding processes is an important part of modern product development. Simulation allows predictions of filling patterns, air traps, warpage, weld lines and fiber orientations, among other physical phenomena involved. This calls for the need of robust and realistic simulation methods to model injection molding. As a result, a lot of recent work has been done to investigate appropriate modeling and simulation methods for injection molding simulations[1–4].

Most established approaches for this are focused on mesh based methods, including both finite-element [2,5–7] and finite-volume-methods[8–10]. These methods are state of the art in modern commercial solutions for injection molding, and they can solve most applications robustly. The quality of the results as well as the computational efficiency however depend on the user-defined mesh. This meshing process can prove to be very time-consuming due to the complex geometries representing the mold being filled. Furthermore, the modeling of free surfaces and associated phenomena, such as the fountain flow effect, is only possible to a limited extent with mesh-based methods. The prediction of fiber distributions and orientations with mesh-based methods also poses several challenges, as the treatment of heterogeneous distributions is only possible indirectly. Since mesh-based methods are typically limited to fixed Eulerian frameworks, the extra effort needed for the convective terms of the fiber orientation models can make the already complex models quite cumbersome.

To avoid these issues with simulating injection molding processes with mesh-based methods, recent literature has explored the use of novel approaches that are free of a user-defined mesh. Bertevas et al.[11] used the meshfree smoothed particle hydrodynamics for the simulation of 3D-printing of a polymer liquid. Among other widespread applications of SPH[12,13], Fan et al.[14] applied SPH to the modeling of simple injection molding scenarios. Another study by He et al.[15] uses SPH to model injection molding flows with a novel formulation for fiber orientations in short fiber reinforced polymers. Wu et al. have a closely related scope in[16], using SPH for injection molding and discrete element method for fiber orientation. These studies have shown the general applicability of meshless methods to injection molding by enabling a realistic modeling of flow patterns. This preliminary work has also been extended by several authors to consider more sophisticated models for injection molding. Xu and Yu[17,18] also include the consideration of pressure and temperature distributions. Recently, Ren et al.[3] have used an improved SPH method to simulate simple injection molding cavities, showing good agreement to the commercial injection

molding software Moldflow. Put together, these studies have illustrated that the conventional advantages of SPH also carry over to the present case. Most important is the ease of handling of free surface flow, and the accuracy due to the Lagrangian interpretation of convective terms.

Several challenges in SPH also carry over to the present application. Most important among these is the difficulty in handling complex boundary conditions. The instability of SPH methods at high injection pressures also requires special treatment. These persistent challenges may be a reason that only simplified flow simulations have been published to date. To the authors' knowledge no meshfree simulations of injection molding processes have been done that consider a fully coupled material, having shear rate and temperature depended viscosity, density, and heat capacity with latent heat and thermal conductivity also considered. The aim of the present work is to develop a meshfree simulation framework that can accurately model these complex material properties.

To avoid the aforementioned challenges inherent in the SPH formulation, we shall use an alternative mesh free method, called the finite pointset method (FPM). First proposed by Kuhnert[19], FPM has the same advantages as SPH regarding free surface flows but enables a direct handling of boundary conditions due its collocation nature based on the generalized finite difference method (GFDM). This method has been successfully used in numerous applications like water crossing of vehicles[20], soil mechanics[21] and solution mining[22]. Reséndiz-Flores et al.[23] applied FPM to the modeling of mould filling processes for metal casting. This study is closely related to injection molding and has proven the general applicability of FPM to this field. However, the shear thinning behavior and thermal effects relevant in injection molding has not yet been considered by Reséndiz-Flores et al.[23].

Other mesh free approaches, e.g. the particle finite element method (PFEM) have also been developed, showing promising results in applications like mould filling in metal casting, glass forming and melting of polymers[24–26]. However, to the authors knowledge, no PFEM application to injection molding has been published. Unlike methods like PFEM, the meshfree FPM used here is a purely meshfree method, without the need of a background grid.

In this work, we present a meshfree approach based on the FPM, to accurately model injection molding processes. Due to their high relevance, all characteristic material properties will be considered in a thermal coupled model. The novelty of the present work lies in both the numerical framework used and the complexity of the material models in a mesh free approach for injection molding. The developed numerical framework will be evaluated against reference models.

In addition, extensive experimental studies are carried out, on the basis of which the simulated flow behavior is evaluated as a function of temperature and the material used. In most previous studies on mesh-free injection molding simulations, no experimental data were used to validate the method.[3,14,15] Only Xu and Yu[17,18] used experimentally observed flow patterns to validate their method. However, simplified material models for the polymer were used in their studies. Therefore, to the authors' knowledge, this is the first time that the flow behavior of a mesh free injection molding method using a complex material model is experimentally validated beyond the flow pattern. Furthermore, aforementioned meshfree methods have only been applied to simplified geometries. No filling processes of industrially relevant components could be simulated with mesh-free methods so far. In the present study, the FPM method is applied to the filling process of a current vehicle component.

II. INJECTION MOLDING

Injection molding is the most important primary molding process in the production of plastic components, and the most commonly used continuous process for the fully automated production of mass-produced plastic components at low costs. It offers an enormous freedom of design and allows the production of one or more complex shapes and contours in a single step with very short cycle times.

With an estimated global market of $265.1 billion (2020) and an estimated average annual growth rate of 4.6% through 2028, demand for plastic components produced by injection molding is expected to grow steadily[27]. At the same time, the use of glass fiber reinforced plastics for injection molding will play an even greater role in the future[27].

The injection molding process is divided into four phases[28]: dosing and plasticizing, injection, packing and cooling, and demolding. In the first step, the plastic, which is usually in granular form, is fed through a hopper into the rotating screw of the injection molding machine and conveyed toward the tip of the screw. There, the granulate is plasticized into a homogeneous melt by heating with the aid of heating elements and the heat generated by the shearing occurring in the screw. In the injection phase, the compressed polymer melt is injected into the mold by opening the nozzle while the screw is moving forward translationally.The melt then cools down in the mold and solidifies. In the final molding step, the mold is opened and the finished component can be removed. In the present work, we focus on the simulation of the injection phase of the injection

molding process, as this is the processing step with the greatest need for simulation. This process step takes only a few seconds in the vast majority of industrial applications. Thus, it is assumed, that the heating of the steel tool only occurs to a small extend. As a result, cooling channels are not considered in the models used in the present work, since they are not expected to significantly affect the flow behavior.

In order to make a prediction about the melt behavior in the cavity during an injection molding process, injection molding simulations are applied in practice. They allow predictions of filling patterns, air traps, warpage, weld lines and fiber orientations, among other attributes of the process. In this way, the gate positions, cooling channel dimensions, wall thicknesses or temperature control parameters can be determined before the first mold prototypes are produced[29].

The injection molding process involves several complex physical processes combined with complex material properties of the polymer melt. These two things pose a challenge in the modeling and simulation of injection molding processes. In order to realistically simulate the melt behavior, knowledge of the material parameters that determine the flow behavior of the melt, like the viscosity, the specific heat capacity and the thermal conductivity are necessary. Among other physical phenomena, the effect of shear thinning, which describes the dependency of viscosity on shear rate is highly important. In this context, an important challenge in simulations is the representation of the nonlinear dependence of the material parameters on pressure and temperature in the material models used. On the other hand, the shear thinning behavior is the basis for using high injection pressures which in turn lead to high shear rates in order to fill even complex cavities with fine structures within seconds. In addition to the complex material behavior, there are process-related challenges such as phase change, crystallization, rapid cooling rates and time-varying boundary conditions which represent a further challenge in the simulation process[29,30]. In the present work, we present a model that takes all these complexities into account.

III. MATHEMATICAL MODEL

In this section, we describe the basic fluid flow equations and boundary conditions used to model the injection molding processes, and the required extensions to accurately capture the flowing polymer melts. We also explain the closure relation for the specific volume, and the viscosity model to capture the shear thinning behavior.

A. Conservation Equations

The basic governing equations are the standard conservation equations of mass, momentum and energy, written in a Lagrangian formulation.

$$\begin{aligned} \frac{d\rho}{dt} &= -\rho \cdot \nabla^{\mathrm{T}} \mathbf{v}, \\ \frac{d\mathbf{v}}{dt} &= \frac{1}{\rho} \cdot (\nabla^{\mathrm{T}} \mathbf{S})^{\mathrm{T}} - \frac{1}{\rho} \cdot \nabla p + \mathbf{g}, \\ (\rho \cdot c_{\mathrm{v}}) \cdot \frac{dT}{dt} &= \nabla^{\mathrm{T}}(\mathbf{S} \cdot \mathbf{v}) - (\rho \cdot c_{\mathrm{v}}) \cdot \nabla^{\mathrm{T}} \mathbf{v} - p \cdot \nabla^{\mathrm{T}} \mathbf{v} + \nabla^{\mathrm{T}}(\lambda \cdot \nabla T), \end{aligned} \tag{1}$$

with density ρ, velocity $\mathbf{v} \in \mathbb{R}^3$, stress tensor $\mathbf{S} \in \mathbb{R}^{3x3}$, pressure p, gravity and other body forces $\mathbf{g} \in \mathbb{R}^3$, total energy E, heat capacity c_{v}, temperature T and heat conductivity λ. The material derivative are given by $\frac{d}{dt} = \frac{\partial}{\partial t} + \mathbf{v}^{\mathrm{T}} \nabla$. Furthermore, $\nabla = (\frac{\partial}{\partial x}, \frac{\partial}{\partial y}, \frac{\partial}{\partial z})^{\mathrm{T}}$ is the gradient operator, and ∇^{T} represents the divergence operator. The stress tensor is defined by

$$\mathbf{S} = \eta \cdot \left(\nabla \mathbf{v}^{\mathrm{T}} + (\nabla \mathbf{v}^{\mathrm{T}})^{\mathrm{T}} - \frac{2}{3} \cdot \left(\nabla^{\mathrm{T}} \mathbf{v} \right) \cdot \mathbf{I} \right). \tag{2}$$

B. State Equations

Since polymer melts have a highly variable density, which depends in particular on pressure and temperature, it is necessary to model these relationships for an injection molding simulation. Therefore, in this study, the *2-domain-Tait-pvt*-Equation[31] is used to model the density. In this model, the phase transition is represented by a separation into the liquid and solid state. It has been shown that the density of polymers can be well approximated with this model[32,33]. The basic equation of this model for the specific volume $v = \frac{1}{\rho}$ is

$$v(T,p) = v_0(T) \cdot \left[1 - 0.0894 \cdot \ln \left(1 + \frac{p}{B(T)} \right) \right] + v_t(T,p). \tag{3}$$

where p is the pressure and the remaining factors are evaluated by

$$v_0(T) = \begin{cases} b_1^s + b_2^s \cdot (T - b_5) & \text{for } T \leq T_S \\ b_1^m + b_2^m \cdot (T - b_5) & \text{for } T > T_S. \end{cases} \tag{4}$$

$$B(T) = \begin{cases} b_3^s \cdot e^{[-b_4^s \cdot (T - b_5)]} & \text{for } T \leq T_S \\ b_3^m \cdot e^{[-b_4^m \cdot (T - b_5)]} & \text{for } T > T_S \end{cases} \tag{5}$$

$$v_t(T,p) = \begin{cases} b_7 \cdot e^{b_8 \cdot (t-b5) - b_9 \cdot p} & \text{for } T \leq T_S \\ 0 & \text{for } T > T_S \end{cases} \tag{6}$$

The parameters $b_1^s, b_1^m, b_2^s, b_2^m, b_3^s, b_3^m, b_4^s, b_4^m, b_5, b_6, b_7, b_8$ and b_9 are used to model the properties of a particular material. Thus, these equations form a coupling of the density of the fluid to the temperature and the acting pressure. The values of these parameters for the materials considered in the present work, which can be determined using a density gradient column, are summarized in Table IV in Appendix A.

C. Viscosity

To model the flow behavior of a polymer, it is essential to model the viscosity correctly. As with a large number of materials, the viscosity of a polymer melt depends on the temperature. A higher temperature causes a decrease in viscosity. In experiments, this variation is typically measured in high pressure capillary rheometers. A characteristic property of polymer melts that must be modeled is the shear thinning behavior. This can be described with a strain rate dependence of the viscosity, where the viscosity decreases as the strain rate $\dot{\gamma}$ increases. Note that we have $\dot{\gamma} = \sqrt{\frac{1}{2}\dot{\gamma} : \dot{\gamma}}$ where $\dot{\gamma} = \nabla \mathbf{v}^{\mathrm{T}} + (\nabla \mathbf{v}^{\mathrm{T}})^{\mathrm{T}}$.

In this work, the *Cross-WLF*-Model is used for the viscosity[34] A variety of models have been developed to represent the viscosity behavior of a material, with the *Cross-WLF*-Model becoming the most common for use in commercial injection molding simulation software. For this reason, the *Cross-WLF*-Model, which represents the material behavior described above, is chosen in this work:

$$\eta(\dot{\gamma}, T) = \frac{\eta_0(T)}{1 + (\frac{\eta_0(T) \cdot \dot{\gamma}}{\tau^*})^{(1-n)}}, \tag{7}$$

$$\eta_0(T) = D_1 \cdot exp\left[-\frac{A_1 \cdot (T - D_2)}{A_2 + T - D_2} \right]. \tag{8}$$

D_1 is the viscosity at a reference temperature and n, τ^* D_2, A_1, A_2 are material parameters. The values of these parameters for the materials considered in the present work are summarized in Table V in Appedix A.

D. Thermal Properties

The thermal properties, heat capacity and thermal conductivity, are given in tabular form as a function of temperature. These values can be measured using differential scanning calorimetry. The corresponding values for both materials in this study can be found in Appendix A. The transition from liquid to solid state does not need special handling, as it is covered by the used material models.

E. Boundary Conditions

One of the advantages of using the present discretization method over other meshfree methods such as SPH is the ease of imposing a variety of boundary conditions directly. In particular, here, the interaction between the polymer melt and the mold walls can be handled naturally, without any extra effort. The boundary conditions used in this study are presented in the following.

For the velocity, a no slip boundary condition is used at the mold walls while a constant inflow velocity is defined at the gate, representing a constant inflow volume flux of polymer melt. The free surface boundary conditions for the velocity are given by a stress evaluation in the normal and tangential directions[35]

$$\mathbf{t}_1^{\mathrm{T}} \cdot \mathbf{S} \cdot \mathbf{n} = 0 \tag{9}$$

$$\mathbf{t}_2^{\mathrm{T}} \cdot \mathbf{S} \cdot \mathbf{n} = 0 \tag{10}$$

$$\mathbf{n}^{\mathrm{T}} \cdot \mathbf{S} \cdot \mathbf{n} = p - p_0 - \sigma\kappa \tag{11}$$

where $\mathbf{t_1}$ and $\mathbf{t}_2$ are orthonormal free boundary tangents, $\mathbf{n}$ is the outward pointing boundary normal, p_0 is the reference atmospheric pressure, σ is the surface tension, and κ is the boundary curvature.

The pressure at the inflow gate and the mold wall is controlled by a homogenous Neumann boundary condition

$$\frac{\partial p}{\partial \mathbf{n}} = 0. \tag{12}$$

The temperature at the inflow is assumed to be a constant value $T_{injection}$. A Robin boundary condition is imposed on the temperature field at the mold walls

$$-\lambda \cdot \frac{\partial T}{\partial \mathbf{n}} = \xi \cdot (T - T_{wall}) \tag{13}$$

where λ is the thermal conductivity of the material, T_{wall} is the assumed mold temperature and ξ is a proportionality coefficient for the convective heat flux. The value of this coefficient is set to $\xi = 5000$ for this study, which is within the range found in the literature[36]. At the free surface, the temperature is computed as the average of the surrounding points.

IV. NUMERICAL SCHEME

A coupled velocity-pressure scheme is used to solve the conservation equations. In following, the time integration scheme is presented, followed by the developed approach for energy correction. Finally, the meshfree discretization procedure is explained.

A. Time Integration

The following description details the process of time integration from time level $t^{(n)}$ to $t^{(n+1)}$. The time integration procedures starts with a Lagrangian update of particle positions with the velocity using a second order method[37].

$$\mathbf{x}^{(n+1)} = \mathbf{x}^{(n)} + \mathbf{v}^{(n)} + \frac{1}{2}\frac{\mathbf{v}^{(n)} - \mathbf{v}^{(n-1)}}{\Delta t_0} \cdot \Delta t^2 \tag{14}$$

where the current time step is given by $\Delta t = t^{(n+1)} - t^{(n)}$ and the previous time step value is $\Delta t_0 = t^{(n)} - t^{(n-1)}$.

The temperature is solved by a semi-implicit time integration. To simplify notation, the indices of the point cloud are omitted below. The discrete temperature system is given by

$$(\mathbf{I}_T + \mathbf{D}_T) \cdot T^{(n+1)} = (\rho^{(n)} \cdot c_{\mathrm{v}}^{(n)}) \cdot T^{(n)} + \mathbf{f}_T, \tag{15}$$

where

$$\begin{aligned} \mathbf{I}_T &= \rho^{(n)} \cdot c_{\mathrm{v}}^{(n)} \cdot \mathbf{I}, \\ \mathbf{D}_T &= -\Delta t \cdot \tilde{\nabla}^{\mathrm{T}} \left(\lambda^{(n)} \cdot \tilde{\nabla} \right), \\ \mathbf{f}_T &= \Delta t \cdot \left(\tilde{\nabla}^{\mathrm{T}} \left(\mathbf{S}^{(n)} \cdot \mathbf{v}^{(n)} \right) - \left(\tilde{\nabla}^{\mathrm{T}} \mathbf{S}^{(n)} \right) \cdot \mathbf{v}^{(n)} - p^{(n)} \cdot \tilde{\nabla}^{\mathrm{T}} \mathbf{v}^{(n)} \right). \end{aligned} \tag{16}$$

Here, $\tilde{\nabla}$ denotes the discrete differential operators for the gradient, which are explained in Section IV D. The above linear system is solved for the unknowns $T^{(n+1)}$. All sparse implicit linear systems, including the ones appearing below, are solved with a BiCGSTAB iterative solver[38].

Having determined the new temperature field $T^{(n+1)}$, the physical properties $\rho^{(n+1)}$, $\eta^{(n+1)}$, $\lambda^{(n+1)}$ and $c_{\mathrm{v}}^{(n+1)}$ are updated using the definitions in Sect. III and Appendix A.

The pressure field is split into hydrostatic and dynamic components[20,39], which are considered separately:

$$p = p_{\mathrm{hyd}} + p_{\mathrm{dyn}}. \tag{17}$$

No body forces are taken into account in the present application of injection molding. For the test cases with no gravity, we have $p_{\mathrm{hyd}} = 0$. When gravity effects are also included, we first update the hydrostatic pressure by

$$\tilde{\nabla}^{\mathrm{T}} \left(\frac{1}{\rho^{(n+1)}} \cdot \tilde{\nabla} p_{\mathrm{hyd}}^{(n+1)} \right) = \tilde{\nabla}^{\mathrm{T}} \mathbf{g}. \tag{18}$$

Note that the hydrostatic pressure does not depend on the velocity, and thus $p_{\mathrm{hyd}}^{(n+1)}$ can be computed without the knowledge of the updated velocity $\mathbf{v}^{(n+1)}$.

The velocity and dynamic pressure are computed using a coupled projection approach[20,39]. For this, a pressure guess will be used

$$\hat{p} = p_{\mathrm{hyd}}^{(n+1)} + p_{\mathrm{dyn}}^{(n)}. \tag{19}$$

The coupled system is then solved by a penalty formulation[39,40]. The divergence of velocity $\tilde{\nabla}^{\mathrm{T}} \mathbf{v}^{(n+1)}$ is used by solving the first equation in equation (1). The discrete system of equations from equation (1) is built up, which is then solved for the unknown correction pressure $p_{\mathrm{corr}}^{(n+1)}$ and intermediate velocity $\hat{\mathbf{v}}^{(n+1)}$:

$$\begin{aligned} \left(\mathbf{I} - \frac{\Delta t}{\rho^{(n+1)}} \cdot \tilde{\psi}_{\hat{\eta}^{(n+1)}}^{(n+1)} \right) \cdot \hat{\mathbf{v}}^{(n+1)} + \frac{\Delta t}{\rho^{(n+1)}} \cdot \tilde{\nabla} p_{\mathrm{corr}}^{(n+1)} &= \mathbf{v}^{(n)} - \frac{\Delta t}{\rho^{(n+1)}} \cdot \tilde{\nabla} \hat{p} + \Delta t \cdot \mathbf{g}, \\ \tilde{\nabla}^{\mathrm{T}} \left(\frac{\Delta t_{\mathrm{virt}}}{\rho^{(n+1)}} \cdot \tilde{\nabla} p_{\mathrm{corr}}^{(n+1)} \right) &= \tilde{\nabla}^{\mathrm{T}} \hat{\mathbf{v}}^{(n+1)} - \tilde{\nabla}^{\mathrm{T}} \mathbf{v}^{(n+1)}, \end{aligned}$$

with

$$(\tilde{\psi}^{(n+1)}_{\hat{\eta}^{(n+1)}})^{\mathrm{T}} = \tilde{\nabla}^{\mathrm{T}}(\hat{\eta}^{(n+1)} \cdot \tilde{\nabla}) \cdot (\hat{\mathbf{v}}^{(n+1)})^{\mathrm{T}} + (\tilde{\nabla}\hat{\eta}^{(n+1)})^{\mathrm{T}} \cdot (\tilde{\nabla}(\hat{\mathbf{v}}^{(n+1)})^{\mathrm{T}})^{\mathrm{T}} + \frac{\hat{\eta}^{(n+1)}}{3} \cdot (\tilde{\nabla}(\tilde{\nabla}^{\mathrm{T}}\hat{\mathbf{v}}^{(n+1)}))^{\mathrm{T}} - \frac{2}{3} \cdot (\tilde{\nabla}^{\mathrm{T}}\hat{\mathbf{v}}^{(n+1)}) \cdot (\tilde{\nabla}\hat{\eta}^{(n+1)})^{\mathrm{T}},$$

and $\Delta t_{\mathrm{virt}} = A_{\mathrm{virt}} \cdot \Delta t$, $0 \leq A_{\mathrm{virt}} \leq 1$. The characteristics of the system of equations depend on A_{virt}. $A_{\mathrm{virt}} = 0$ would give the exact solution, however, this value is not used because the resultant linear system would then be ill-conditioned. With $0.001 \leq A_{\mathrm{virt}} \leq 0.1$ a good balance can be found here[40].

Finally, the velocity and dynamic pressure are updated by

$$\begin{aligned} \mathbf{v}^{(n+1)} &= \hat{\mathbf{v}}^{(n+1)} - \frac{\Delta t_{\mathrm{virt}}}{\rho^{(n+1)}} \cdot \tilde{\nabla} p^{(n+1)}_{\mathrm{corr}}, \\ p^{(n+1)}_{\mathrm{dyn}} &= p^{(n)}_{\mathrm{dyn}} + p^{(n+1)}_{\mathrm{corr}}. \end{aligned} \tag{20}$$

For more details, and numerical verification and validation of the overall time integration procedure, we refer the reader to our earlier work[20,21,35,40–43].

B. Energy Conservation

Since thermal effects play a major role in injection molding, it is essential to model the energy correctly in injection molding simulations. However, meshfree methods often require extra work to ensure conservative behavior[35,44,45]. Due to their inherent local nature, without a global mesh to balance fluxes, locally accurate discretizations can still lead to globally unconservative behavior. This holds true for not just the GFDM / FPM approach used in the present work, but also for other meshfree approaches such as SPH. To maintain a global energy balance in the discrete system, we introduce a correction mechanism described below. We start by the considering the global or integral form of the energy balance equation

$$\frac{d}{dt}\int_{\Omega} \rho \cdot c_v \cdot T = -\int_{\delta\Omega} (\rho \cdot c_v \cdot T) \cdot (\mathbf{v}^{\mathrm{T}} \cdot \mathbf{n}) + \int_{\delta\Omega} \lambda \cdot ((\nabla T)^{\mathrm{T}}\mathbf{n}) + \int_{\delta\Omega} p(\mathbf{v}^{\mathrm{T}}\mathbf{n}) - \Delta E, \tag{21}$$

where Ω is the computational domain with boundary $\delta\Omega$. The stress tensor term is not included here, since it is assumed that this has a subordinate role for the energy balance in injection molding.

In the above equation ΔE is the missing energy in the injection molding system. This fraction represents the error that occurs during the numerical discretization. Therefore, the goal of the

energy correction process used here is to bring ΔE to zero. For this purpose, a heat source Q is introduced, which supplies the missing energy to the point cloud via a weighting function χ. To increase numerical stability, this energy is to be entered into the system over five time steps. We then get the following heat source

$$Q = \frac{1}{5\Delta t}\Delta E \cdot \frac{\chi}{\int_\Omega \chi}. \tag{22}$$

The weighting function used here is defined as

$$\chi = \begin{cases} 0 & \text{for } T \geq T_{injection} \\ (T - T_{injection})^3 & \text{for } T < T_{injection} \end{cases} \tag{23}$$

As we shall show in section VI D, this procedure helps in ensuring energy conservative behavior of the numerical results.

C. Domain Discretization

We now explain the meshfree domain discretization procedure. The computational domain is discretized with a cloud of points, or a *point cloud*, consisting of $N = N(t)$ points. This includes points in the interior of the domain, and on the boundary of the domain. Unlike particle-based meshfree methods like SPH, here points are not mass-carrying particles. They are simply collocation nodes, or locations where approximations are carried out. For every point $i = 1, 2, \ldots, N$, all numerical computations are performed on a set of nearby points, referred to as the support or neighborhood of point i. This neighborhood is determined by the closest points of i, $S_i = \{\mathbf{x}_j | \, \|\mathbf{x}_j - \mathbf{x}_i\| \leq h_i\}$. Here, $h_i = h(\mathbf{x}_i, t)$ is the smoothing length or interaction radius, which governs both the inter-point distance and the size of the neighborhood[35].

The point cloud is irregularly spaced, and there is no underlying mesh or grid that connects the points. The only connectivity present is the neighborhoods defined above, which can change as the points move in a Lagrangian fashion. While points are irregularly spaced, we maintain a quasi-regularity of points, by ensuring that two points do not come closer than a fixed multiple of h, here $r_{\min} h$, and that there are no holes in the domain of size $r_{\max} h$ where points are missing[35].

D. Spatial derivatives

All discrete derivatives are computed using a meshfree Generalized Finite Different Method (GFDM)[46]. The GFDM is a collocation method that generalizes classical finite differences to arbitrarily spaced point clouds. Consider a function u defined at each point i on the computational domain. The derivatives of u at a point $\mathbf{x}_i$ are given by

$$\nabla u(\mathbf{x}_i) \approx \tilde{\nabla}_i u = \begin{pmatrix} \sum_{j\in S_i} c_{ij}^x u_j \\ \sum_{j\in S_i} c_{ij}^y u_j \\ \sum_{j\in S_i} c_{ij}^z u_j \end{pmatrix}, \tag{24}$$

$$\Delta u(\mathbf{x}_i) \approx \tilde{\Delta}_i u = \sum_{j\in S_i} c_{ij}^\Delta u_j\,, \tag{25}$$

where the $\sim$ denotes the corresponding numerical differential operator. The coefficients c_{ij} are determined using a least squares approach. First, we ensure that a certain set of test functions are differentiated exactly. Here, we consider monomial function, upto a desired order. The resultant under-determined linear system is solved using a weighted norm minimization. Consider, for example, the computation of the discrete Laplacian operator. We get

$$\sum_{j\in S_i} c_{ij}^\Delta m_j = \Delta m(\mathbf{x}_i)\,, \quad \forall m \in \mathscr{M}_p\,, \tag{26}$$

$$\min \sum_{j\in S_i} \left(\frac{c_{ij}^\Delta}{W_{ij}}\right)^2, \tag{27}$$

where $\mathscr{M}_p$ is the set of test functions. Here, we use monomials up to the order $p = 2$. The weighting function W ensures that points closer to the center point i have a larger influence on the derivative computation than points further away. Here, we consider a truncated Gaussian weighting function, which has widely been used in GFDMs

$$W_{ij} = \exp\left(-\alpha \frac{\|\mathbf{x}_i - \mathbf{x}_j\|^2}{h_i^2 + h_j^2}\right), \tag{28}$$

for a positive constant α chosen in the range of $(2,6)$. We refer the reader to to[45,47,48] for more details on derivative computation with GFDMs, and to[49–52] for examples on how GFDMs can be applied.

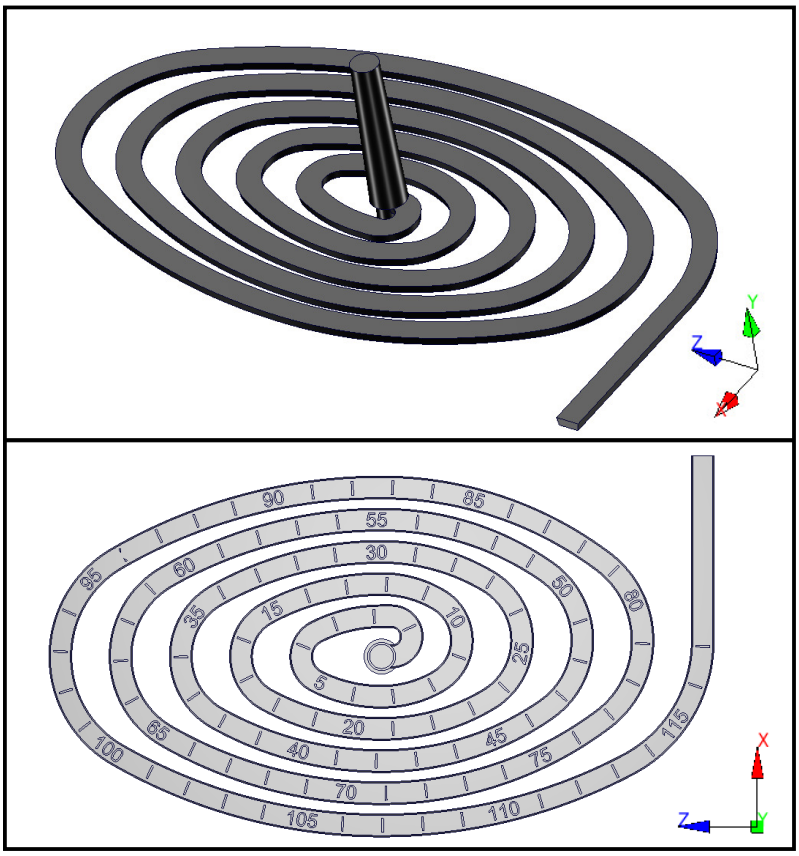

FIG. 1. Mold geometry used in the injection molding experiments

V. EXPERIMENTAL MEASUREMENTS

For a thorough validation of our model and simulations, we also perform injection molding experiments. The design of these experiments is described in this section.

The used mold geometry for the experiments is shown in figure 1. The melt is injected into the spiral mold at the center, through the shown sprue. The sprue has a conical shape with an upper diameter of 6.7mm and a lower diameter of 8.7mm. The rectangular spiral cavity has a width of 5mm and a height of 2mm. The maximum flow length is 1220mm.

We use the experiments for both a quantitative and a qualitative validation of our simulations. The primary measurements conducted in the experiments is the maximum flow path lengths at prescribed injection pressures. As shown in figure 1, the cavity has flow path length markings at 10mm intervals. This allows the length of the fabricated spiral to be measured.

In this study, the experiments are carried out for two materials. Both materials are short glass fiber reinforced polypropylene, with a different mass fractions of glass fiber, one with 25%, and

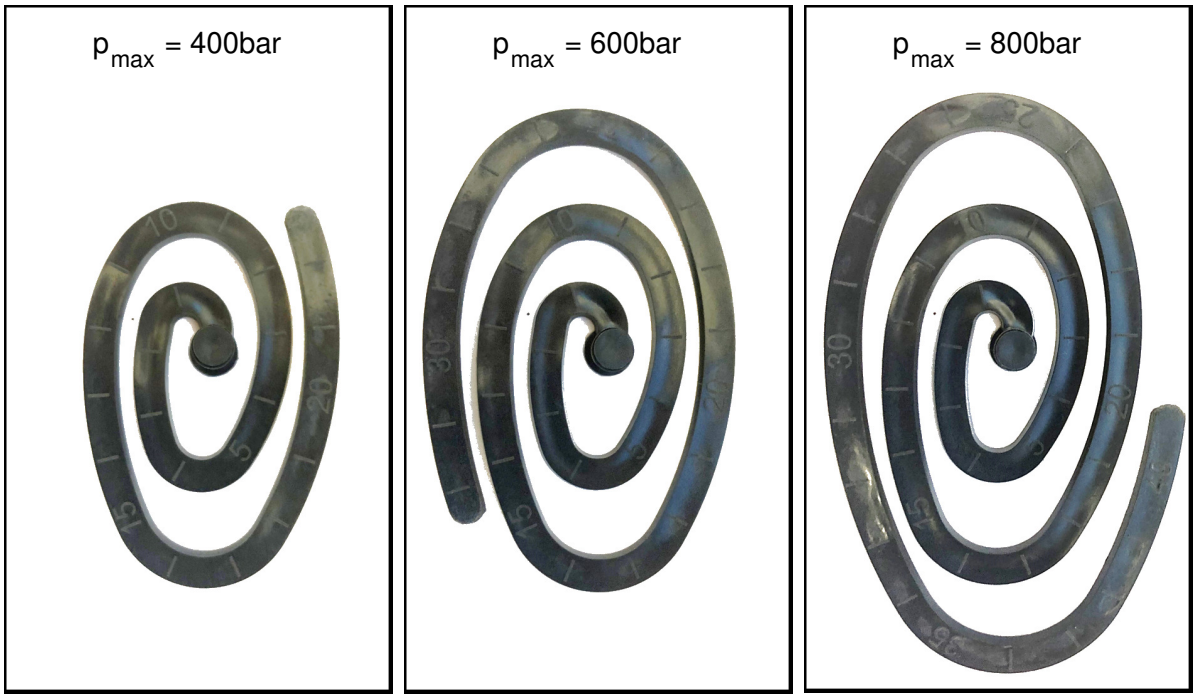

FIG. 2. Molded spirals from experiments for three maximum pressure values

the other with 30%. In the remainder of the text, these materials will be referred to as PPGF25 and PPGF30, where the PPGF stands for polypropylene glass fiber. PPGF25 has a melt flow rate of 15 $\frac{g}{cm^3}$ and PPGF30 of 4$\frac{g}{cm^3}$ according to ISO 1133. Consequently, the PPGF25 has a higher flowability. We note there that these materials are also often used in industrial injection molding processes, including in the glove box door test case considered in section VI E.

The injection molding process is carried out with a constant volume flow. Due to the viscous character of the polymer melt as well as the progressive cooling of the melt, a steadily increasing injection pressure can be observed as the flow length in the mold increases. When a defined threshold pressure is reached, the injection process is stopped. After cooling and ejection of the fabricated sample, its length is determined.

The spiral flow test is performed at varying injection parameters. For all settings examined, three threshold injection pressures are considered. These are $p_1 = 400bar$, $p_2 = 600bar$ and $p_3 = 800bar$. The injection process is controlled by a constant inflow velocity, which results in a volume flow of $v_{vol} = 1E-5\frac{m^3}{s}$. The inflow is stopped once the threshold pressure has been reached.

The two other parameters of the experiment varied are the injection temperature and the wall

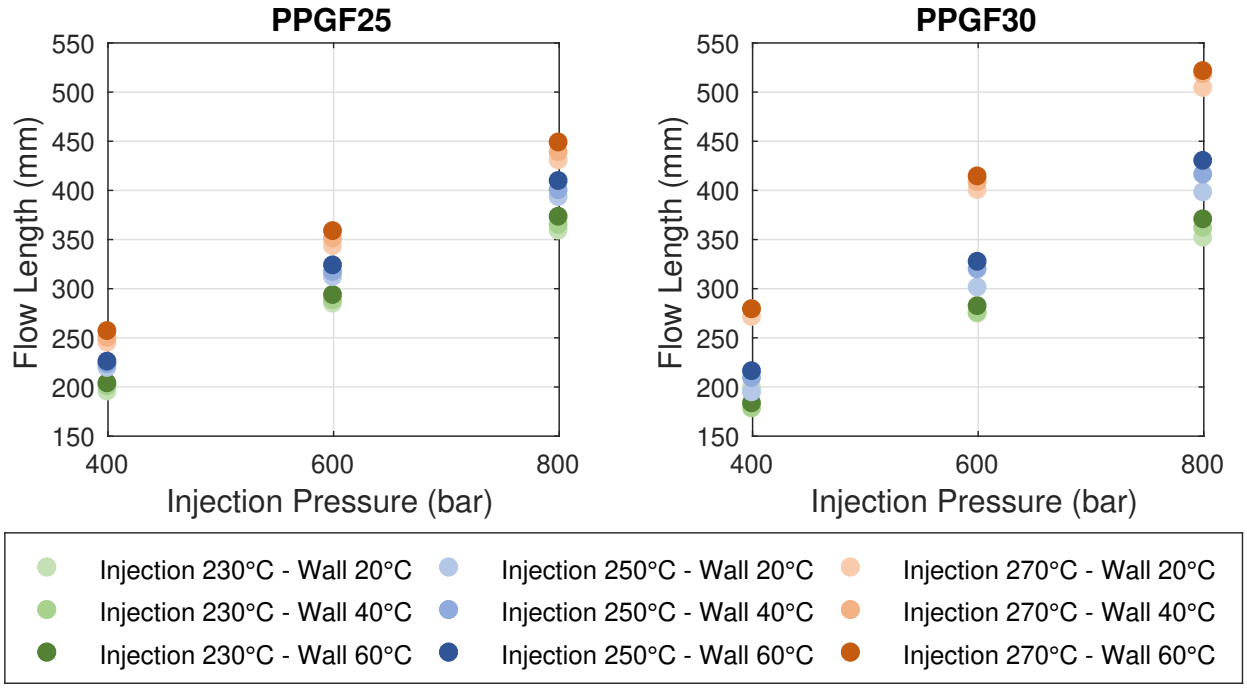

FIG. 3. Results of spiral flow experiments for both materials

temperature of the injection molding tool. These are controlled by the heating elements on the screw and the coolant flow through the mold. In the entire series of tests, the maximum difference between the inflow and outflow temperature of the coolant is $0.5°C$. It is therefore assumed that the influence of the cooling channels on the injection process can be neglected and it has not been taken into account in the simulations.

The different cases considered are shown in table I. These cases represent the range of recommended processing temperatures for the used materials. With the three threshold injection pressures, this leads to a total of 27 different test cases, in each of which the measurements of the flow lengths are carried out for each material: PPGF25 and PPGF30. To reduce the impact of measurement errors, each experiment is repeated 5 times.

In figure 2, three molded spirals are shown. Each using a different maximum pressure. It can be seen how the spiral length increases with higher pressure. The markings on the geometry allow the length to be measured exactly.

The results of the performed experiments are shown in figure 3. This figure displays the average flow length for each parameter configuration across the 5 repetitions. It can be seen, as expected, that with rising injection pressure the flow length increases in each configuration of temperatures. Furthermore, keeping either the wall or the injection temperature fixed, increasing

the other temperature parameter leads to longer flow paths. The effect of injection temperature is more dominant than the variation of wall temperatures. One significant difference in between the two materials is the nonlinear dependency on the injection temperature for PPGF30.

VI. NUMERICAL RESULTS

This section discusses the numerical results using the model and discretization method presented above. Before making comparisons with experimental results, we start by examining simplified models.The simplified test cases in sections VI A and VI B are not directly related to injection molding applications. However, they are used for the initial validation of the method presented here. The numerical stability and suitability of the method for viscous flow problems is illustrated.

A. Poiseuille Flow

As a basic test, the meshfree FPM discretization method as discussed in Section IV is applied to the case of two-dimensional Poiseuille flow, with constant density ρ and viscosity η. This test case is characterized by an initially steady liquid between two fixed walls. The fluid is accelerated by a constant body force F. The analytical solution for this problem can be expressed by the series solution[53]

$$v(y,t) = \frac{F}{2\cdot\nu}\cdot y\cdot(y-L_y) + \sum_{n=0}^{\infty}\frac{4\cdot F\cdot L_y^2}{\nu\cdot\pi^3\cdot(2\cdot n+1)^3}\sin\left(\frac{\pi\cdot y}{L_y}\cdot(2\cdot n+1)\cdot e^{-\frac{(2\cdot n+1)^2\cdot\pi^2\cdot\nu}{L_y^2}}\cdot t\right), \quad (29)$$

TABLE I. Injection and wall temperatures for spiral flow experiments

Test Nb.	Injection Temperature (°C)	Wall Temperature (°C)
1	230	20
2	230	40
3	230	60
4	250	20
5	250	40
6	250	60
7	270	20
8	270	40
9	270	60

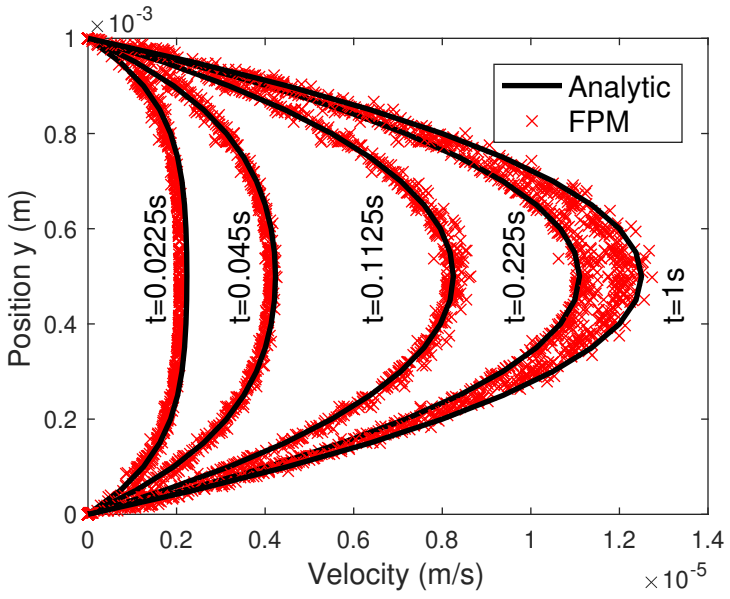

FIG. 4. Results of Poiseuille Flow simulation using FPM compared to analytical results. The vertical axes "Position" refers to the y coordinate of the location. The red crosses represent different locations along the x and z axis for a particular y coordinate

where $v(y,t)$ is the velocity, $0 \leq y \leq L_y$ the vertical position, t the time and $\nu = \frac{\eta}{\rho}$ the kinematic viscosity. The FPM simulation result is compared against this analytical solution. The considered domain is a cuboid of size

$$\begin{pmatrix} L_x \\ L_y \\ L_z \end{pmatrix} = \begin{pmatrix} 0.5mm \\ 1mm \\ 0.5mm \end{pmatrix}, \tag{30}$$

which is discretized with a number of $N \approx 2000$ numerical points using a smoothing length of $h = 0.3mm$. FPM points can pass through the boundaries at $x = 0$ and $x = L_x$. They are created at the inflow boundary and deleted at the outflow. The example can therefore be understood as a section of a channel through which flow occurs. The time step is set to $\Delta t = 1E-3s$. Figure 4 displays these result using the parameters shown in table II. It can be seen that the FPM result is in good agreement with the analytical solution. There is a small scatter within the point cloud, so that fluctuating differences to the analytical solution are present. The average difference for all evaluated time points is $< 7\%$.

For a further verification and validation, including convergence studies, of the FPM discretization and time integration schemes, we refer to our earlier work[20,21,39,41].

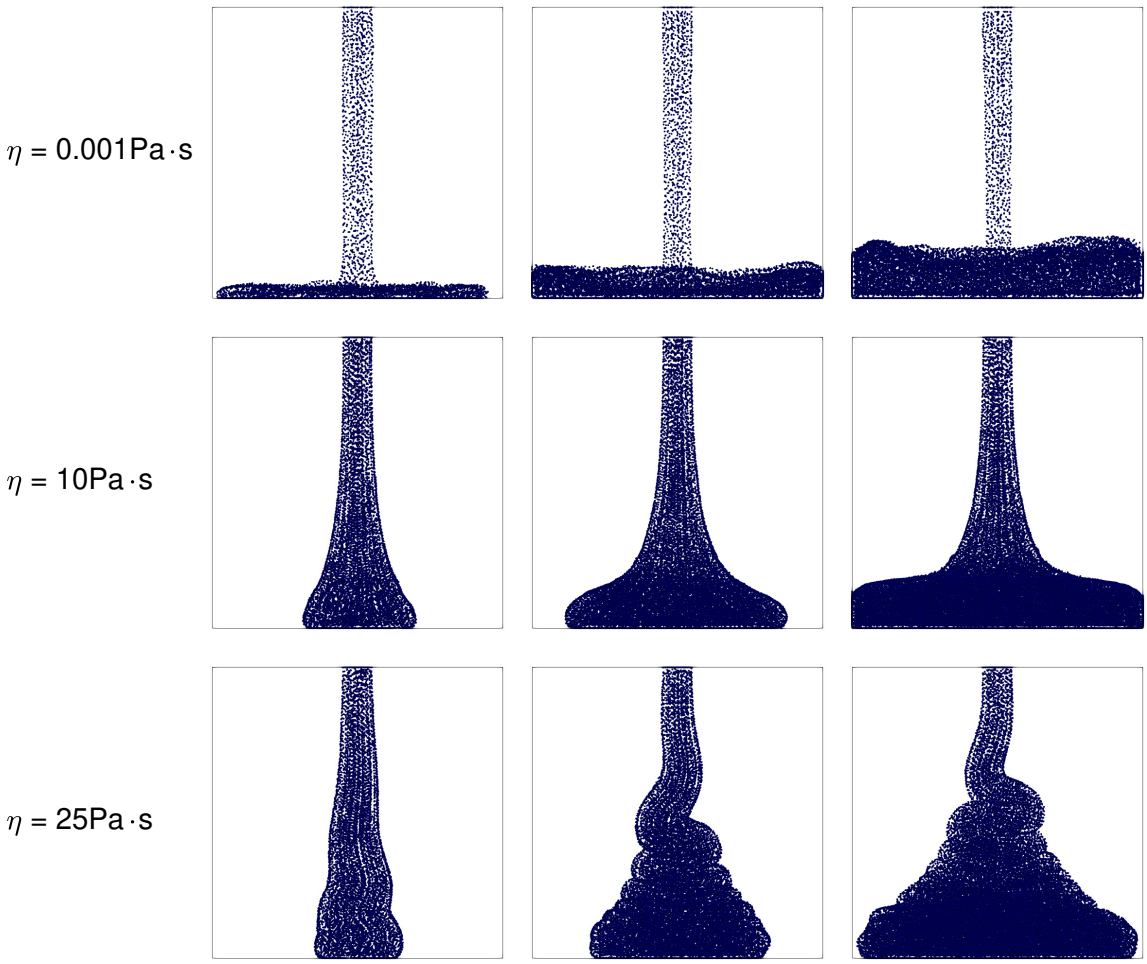

FIG. 5. Jet Injection filling patterns for three different viscosity values

B. Jet Injection

Since the injection molding process of polymers is dominated by their viscosity, the ability of FPM with regard to viscous effects must be investigated. Therefore, a jet injection process with

TABLE II. Parameters for Poiseuille flow simulations. L_y is the length of the channel in the direction of the flow, ν is the kinematic viscosity, F is the external force and ρ is the fixed density.

L_y	0.001m
ν	1E-6 $\frac{m^2}{s}$
F	1E-4 $\frac{m}{s^2}$
ρ	1000 $\frac{kg}{m^3}$

different fluids is considered. The domain under consideration consists of a cube with a volume of $V = 0.001m^3$, on the top of which a circular injection boundary with a diameter of $D = 0.01m$ is present. The inflow velocity is kept fixed at $v_{in} = 1\frac{m}{s}$, while the fluid with a density of $\rho = 1000\frac{kg}{m^3}$ also experiences gravity in vertical direction. A constant viscosity is used in each simulation considered, with the value varied between simulations in order to examine the effect of viscosity in this scenario.

In figure 5 the inflow patterns of three different viscosity values considered is shown in a side view. It is evident that the viscosity has a significant influence on the flow behavior in this scenario. In[54] a theoretical approach for the prediction of buckling of a planar jet has been provided. In this theory, two conditions are given for the occurring of buckling:

$$Re < 0.56 \text{ and } \frac{H}{D} > 3\pi, \tag{31}$$

where Re is the Reynolds number based on the inflow width D and H is the distance between the inflow and bottom surface. In the tested scenario, the second criteria is met, since $\frac{H}{D} = 10 > 3\pi$. The first criteria however depends on the viscosity of the fluid. The corresponding Reynolds numbers for the various viscosities considered are shown in table III. It can be seen that the theoretical limit according to equation 31 can be confirmed with the FPM simulations, as buckling only occurs for the fluid having $Re = 0.4 < 0.56$. Although the used theory is only valid for planar jets, this confirms the ability of FPM to simulate viscous effects robustly.

C. Modeling of fountain flow effect

A major disadvantage of mesh-based methods is that the movement of the melt near the free surface, especially the so called fountain flow effect, can only be modeled by special treatments[55]. In[56] SPH has been used to simulate the fountain flow effect in a simplified test case. In[3] a two

TABLE III. Reynolds Numbers for the tested viscosity values in jet injection model

Viscosity ($Pa \cdot s$)	**Re**
0.001	10000
10	1
25	0.4

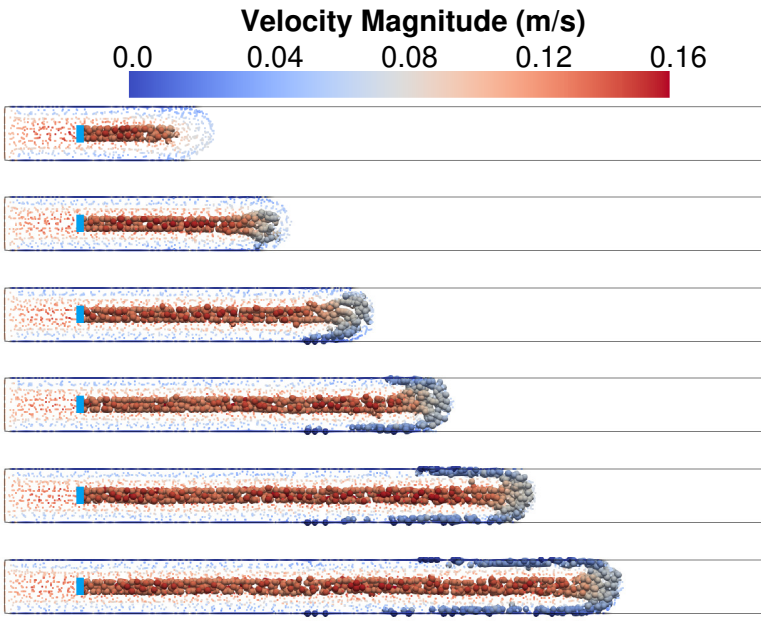

FIG. 6. Visualization of the fountain flow effect in FPM. For the ease of visualization, a larger point size is used for all points passing through the light blue line on the left

dimensional channel flow has been modeled using SPH, showing its abilities to model the fountain flow effect automatically. However, the effect has not been shown using a complex material model having temperature dependence in three dimensional models. Therefore, in this study the ability of FPM for modeling the fountain flow effect is evaluated. Flow of polymer melt through a long thin channel, as shown in figure 6 is considered. A constant inflow velocity of $v_{in} = 0.1\frac{m}{s}$ is used at the inflow, on the left side as visualized by figure 6. The injection temperature is kept fixed at $T_{injection} = 245°C$, while the wall temperature is fixed at $T_{wall} = 40°C$. In this simulation no gravity is present. All material model and boundary conditions applied are as described in section III. For this case, the PPGF25 material is used, for which material parameters are given in Appendix A.

In order to visualize the fountain flow effect, in figure 6 the size of all points passing through the blue line is increased. It can be seen how these points travel steadily towards the free surface. Here, they start moving to the outer walls, creating the typical flow pattern described as fountain flow.

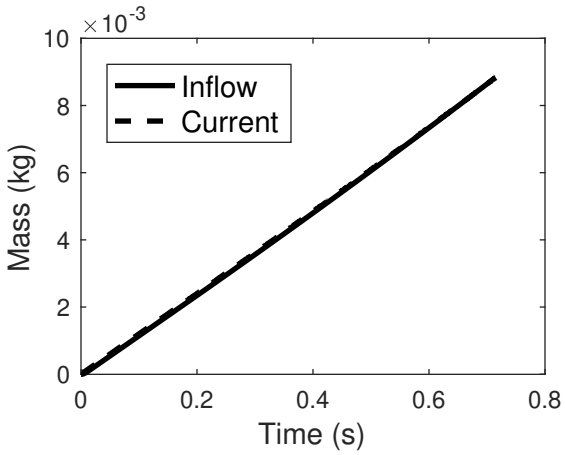

FIG. 7. Comparison of inflow mass and current (numerical) mass in the system for the spiral mold test case

D. Injection Molding Flow of Spiral Mold

In order to validate the flow behavior of the simulated polymer melt, injection in a spiral mold is considered to match our experimental setup used in section V. The primary quantity used for comparing numerical results and experiments is the flow path length as described in section V. Other relevant aspects for a further quantitative and qualitative comparison will also be investigated. No gravity is applied in these models and material parameters can be found in appendix A.

In meshfree collocation methods like FPM and GFDM, conservation of mass and energy can often by troublesome, and must be investigated during the validation of simulations. Figure 7 shows the mass balance of the simulated system, comparing the theoretical mass contained in the system to the numerical mass. According to the characteristics of an injection process, the mass in the system increases linearly over time. The figure shows that the theoretical inflow mass and measured mass in the system lie on top of each other. Thus, the simulation satisfies the conservation of mass.

Figure 8 shows the balance of energy in the system. The sum of the actual energy and the energy dissipated over the edges is nearly identical to the calculated energy flowing into the system. Thereby it can be shown that the methodology used for energy correction introduced in section IV B ensures the conservation of energy in the system.

For the assessment of the flow path length, the simulation results are evaluated when a defined injection pressure is reached. Figure 9 shows the pressure distribution in the spiral when the

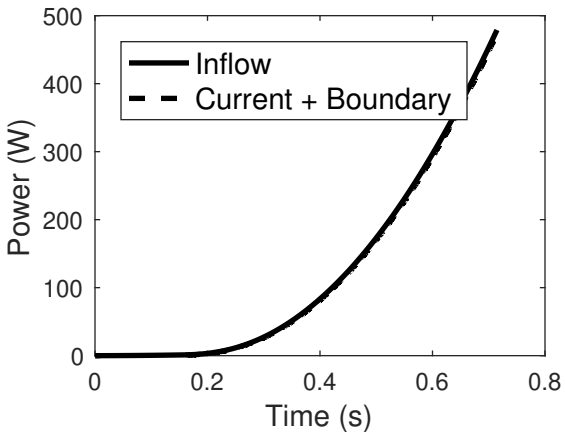

FIG. 8. Comparison of inflow power and current (numerical) power in the system for the spiral mold test case

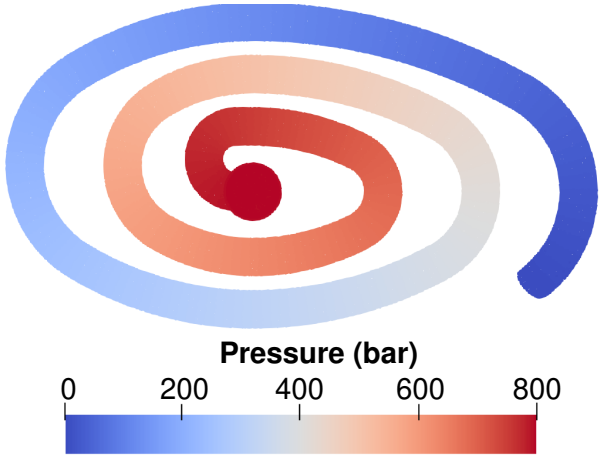

FIG. 9. Pressure field at a maximum injection pressure of 800bar for the spiral mold test case

maximum pressure of 800*bar* is reached. It can be seen that the pressure decreases with increasing distance from the inflow boundary, until a pressure of $p \approx 0\,bar$ prevails on the free surface. The drop in pressure is continuous and thus corresponds to the theoretical expectation.

In figure 10, the increase of injection pressure over the filling time is displayed. It can be seen how the injection pressure initially rises only slightly and after a certain point increases significantly faster. This bend point in the curves corresponds to the transition from the sprue area to the narrower spiral. In order to evaluate the curves, the results of the commercial injection molding software CADMOULD are shown besides. Both results are very close to each other, so that the robustness of the method presented here is evident.

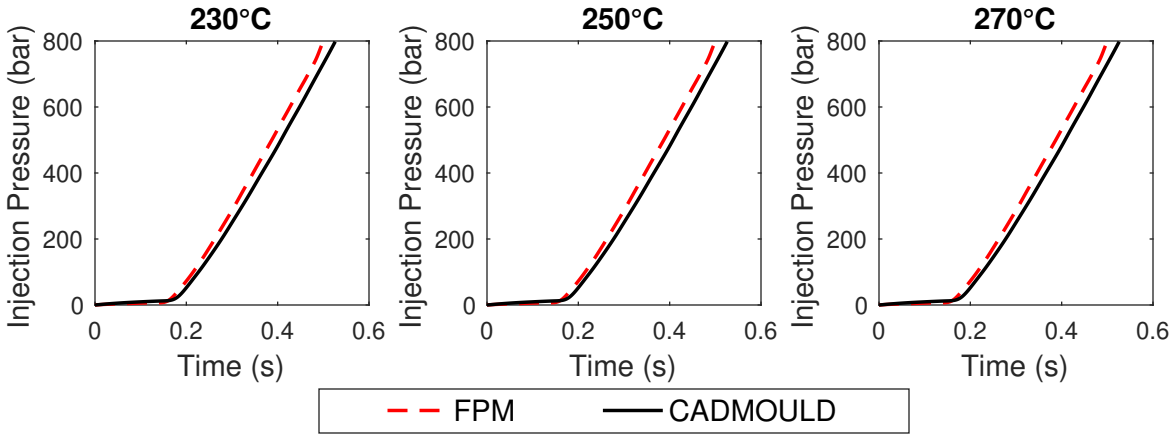

FIG. 10. Comparison of the injection pressure over time calculated by FPM and CADMOULD

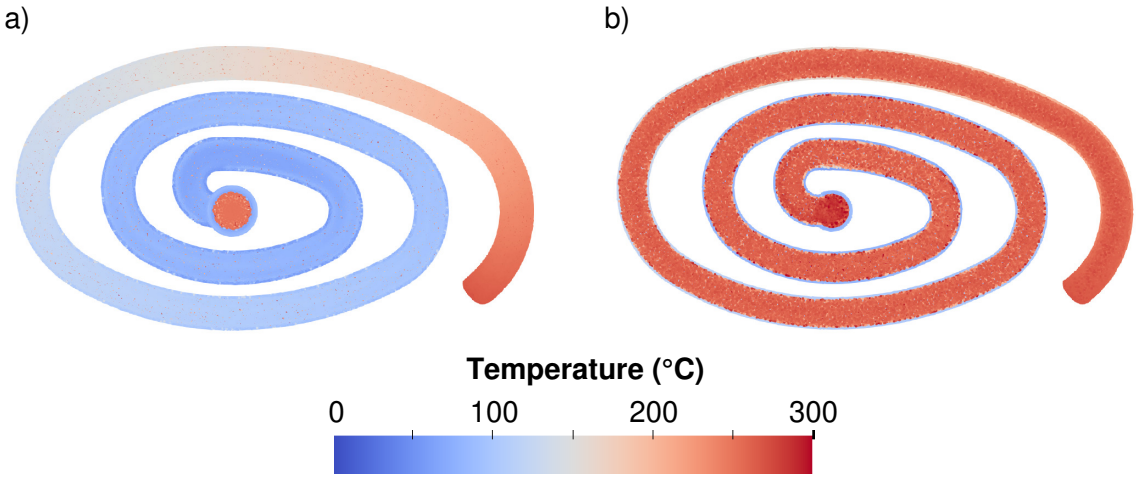

FIG. 11. Temperature field at a maximum injection pressure of 800bar for the spiral mold test case. a) top view on boundary b) cut view at half thickness

As thermal effects are of high relevance for injection molding, the simulated temperature field is evaluated in figure 11. The simulated process has an injection temperature of $T_{injection} = 250°C$ and a wall temperature of $T_{wall} = 40°C$. It can be seen that the interior temperature in the spiral is constant. Towards the outer surface however, there are significant differences. The cold wall leads to a rapid temperature decrease as the melt touches the surface. Since the melt sticks to the surface, the shear velocity increases in adjacent layers. Due to the highly viscous polymer melt, this shear rate causes viscous energy dissipation which leads to an increase in temperature.

For a quantitative validation of the simulations, we now compare the flow path lengths from simulations to measured experimental ones. In figure 12, flow path lengths evaluated by the simu-

lations are shown. By comparing these results to the experimental measurements, shown in figure 3, it becomes evident that the FPM simulations have a high agreement with the experiments. Just as observed in the experiments, increasing the injection pressure increases the flow path length in every temperature configuration. The effect of both the injection and wall temperature are predicted correctly, with the injection temperature playing a larger role in the flow path length than the wall temperature, as also observed in the experiments. For better quantitative comparison between simulation and experiment, the relative difference is evaluated. This value indicating the percentage deviation is given as

$$\Delta l_{rel} = \frac{l_{Experiment} - l_{FPM}}{l_{Experiment}} \cdot 100\%. \tag{32}$$

Figure 12 shows the relative difference for all configurations. The maximum relative difference between the simulated flow path length and the experimental one is 6.74% for PPGF25. For PPGF30, the maximum relative difference is 20.4%. This maximum value occurs at a injection temperature of $T_{in} = 270°C$, while maximum difference for lower injection temperatures is 9.4%. Accordingly, the nonlinear temperature dependence of the flow path is not ideally represented for this material. Nevertheless, it can be concluded that the flow behavior can be calculated for different materials and that the coupling to thermal effects is successful.

The simulation of the spiral mold case was performed on 96 cores, resulting in a computation time of 8 hours. At the maximum flow length, the model used $N \approx 1.8E5$ numerical points

E. Glove Box Door

The previously examined test cases show the fundamental suitability of the presented method for the simulation of injection molding processes. We now show that the presented numerical framework can also be used for complex industrially relevant geometries.

In this test case, FPM is used to simulate the filling process of a glove box door of a current vehicle. The mold has a volume of $v \approx 4E-4m^3$ and with external dimensions of approx. $380mm \times 250mm$. This component is manufactured in a cascade gate, which means that the two existing injection points are time-controlled, so that no weld lines occur. The gate locations are in the top area of the geometry and can be easily identified in figure 13 1). In accordance with the real process, an injection time of $2.7s$, an injection temperature of $260°C$ and a wall temperature of $50°C$ is chosen. The material used is PPGF25. Parameters can be found in appendix A. It is

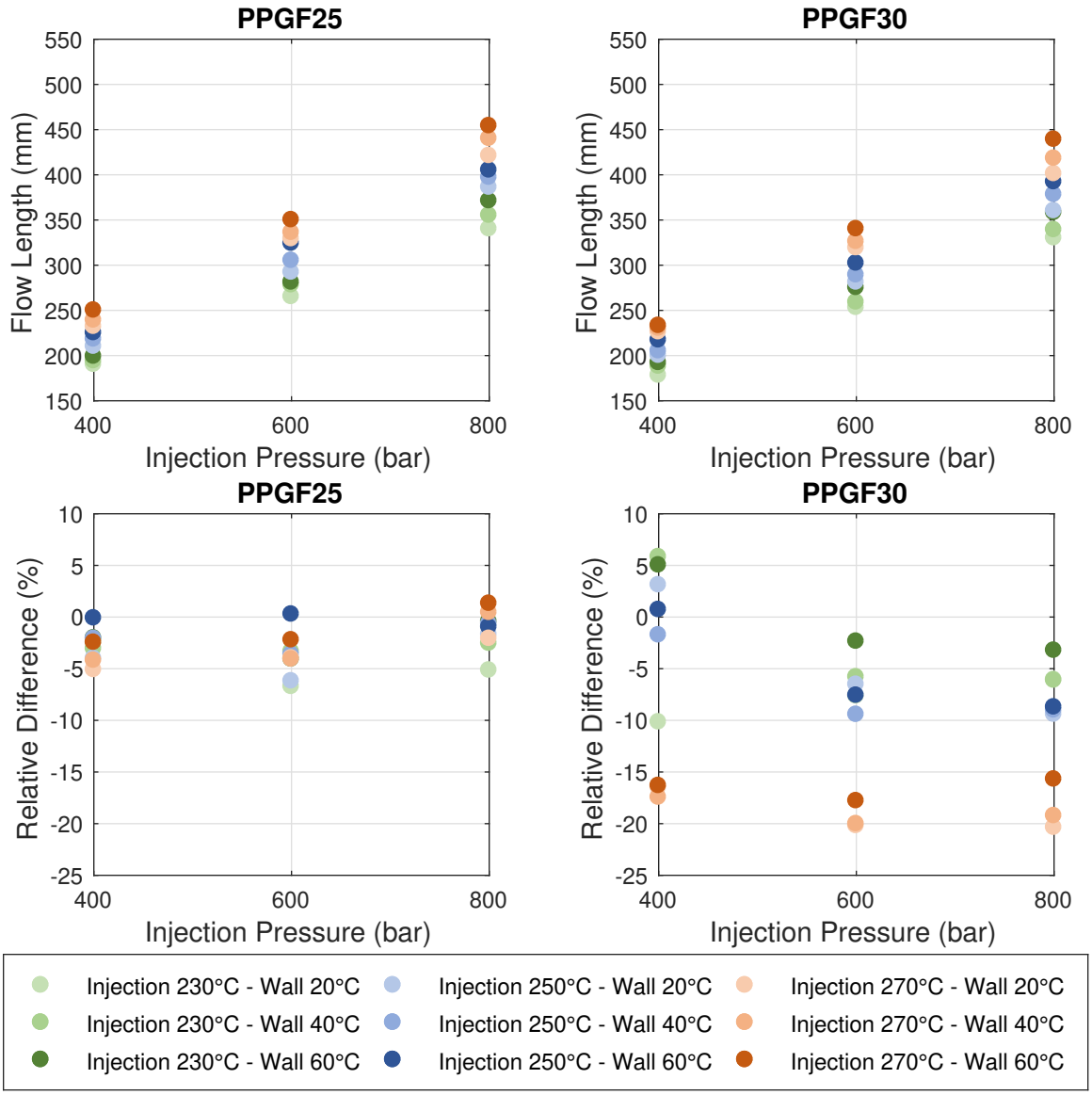

FIG. 12. Results of FPM simulations of the spiral flow for both materials. Bottom pictures are showing the relative difference in flow length compared to experimental results

assumed that the influence of gravity can be neglected for this process, so that no gravity is set in the simulations.

Figure 13 displays the filling patterns simulated by FPM. It can be seen that the cascade gate can be modeled successfully. The movement of the melt front is realistic. As a result, all features of the geometry such as rib reinforcements are completely filled. Thus, the applicability of the method for the injection molding simulation can also be confirmed here.

For a more in-depth evaluation, the FPM simulation is compared with results from the commer-

cial software CADMOULD. This software represents a state of art method for injection molding in indutrial applications. In figure 14 the filling pattern using CADMOULD is shown. The computed temperature differs significantly between both methods. This is due to different thermal boundary conditions at the mold walls. Over all pictures, the comparison of the flow patterns however show only small differences between both methods. Thus, the applicability of the method for the injection molding simulation can also be confirmed here.

The thin-walled structure of this component requires a fine resolution of the point cloud. Unlike mesh based methods, anisotropic domain discretizations are not easily possible in mesh free methods. Thus, the fine resolution required to resolve the thin region must also be used in the tangential direction, despite the much larger length scale there. This is a drawback of not just the meshfree FPM used here, but of all meshfree methods. A smoothing length of $h = 2mm$ is chosen that results in $N \approx 1.7E6$ points present when the cavity is filled completely. This increases the computing effort, which leads to a computing time of 90 hours with a parallelization on 280 cores. This aspect is a disadvantage compared to the established mesh-based methods.

VII. CONCLUSIONS

In this work, the meshfree Finite Pointset Method (FPM), which uses the generalized finite difference method (GFDM), has been applied to simulate injection molding processes.

A complex material model was implemented for comparison with real injection molding processes. This takes into account the compressible behavior based on a *2-domain Tait-pvt* model, as well as the shear thinning behavior using the *Cross-WLF* model for viscosity. Furthermore, the temperature dependence of viscosity, density, heat capacity and thermal conductivity is considered. Compared to previous work, this is the most comprehensive depiction of polymer material behavior with a mesh free method and is comparable with commercial mesh-based methods.

Due to the thermal coupling, the energy balance is of high relevance in this application. Therefore, an approach to correct the energy in the system was developed and validated.

An experimental basis for the evaluation of the FPM simulations was created with flow spiral tests. A spiral cavity was filled with two materials at variable melt and wall temperatures. The comparison of the flow paths covered at defined pressure values shows that the FPM simulations have reasonable agreement with the tests carried out. It could be proven that the non-Newtonian flow behavior can be simulated taking into account the influence of temperature. The material

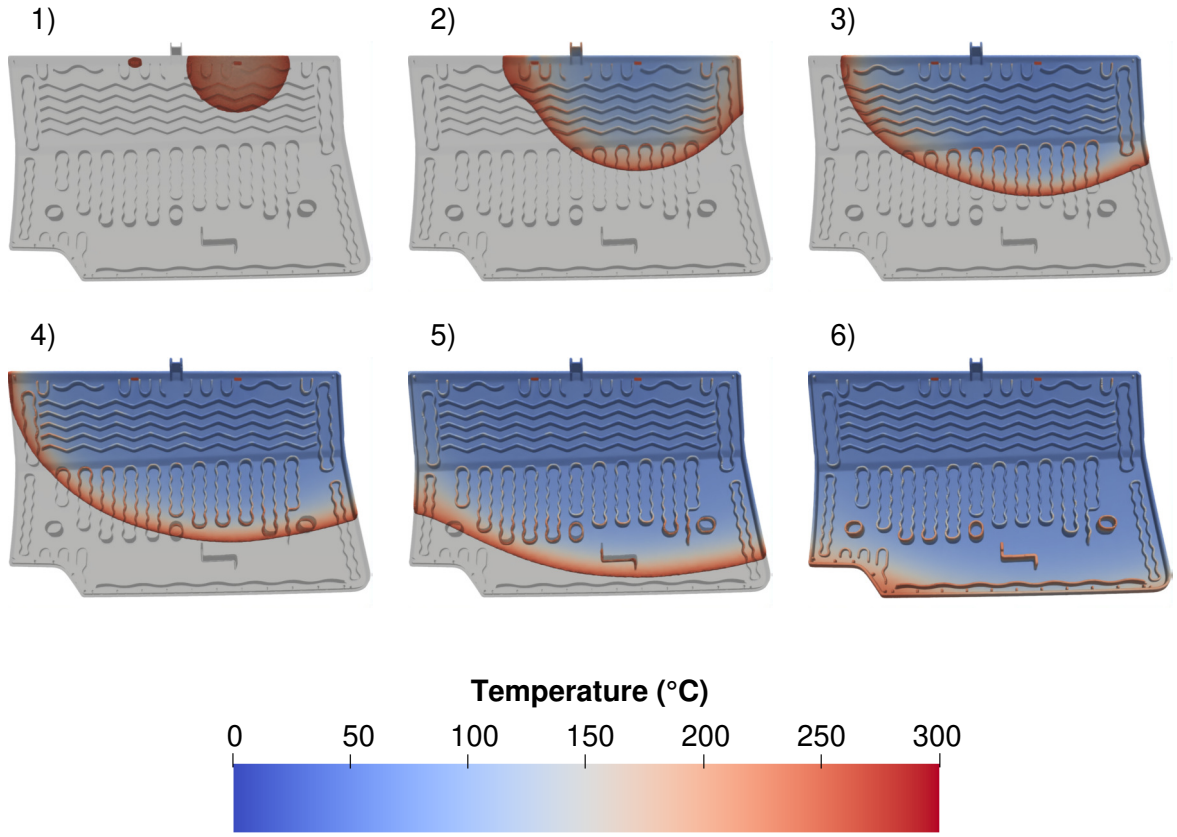

FIG. 13. Filling pattern of injection molding process for glove box door

models considered allow various different materials to be modeled.

Finally, the method was used to simulate the filling process of a glove box door, using a geometry actually used in the automotive industry. A peculiar feature of the process is that the two injection points are opened in a cascade. The realistic pattern image shows the suitability of the method for the simulation of industrial injection molding processes. However, this is accompanied by a relatively high computational effort in large part due to the lack of an anisotropic discretization. In future work, this aspect should be further optimized.

The used method has starting points to compute engineering-relevant aspects such as the localization of weld lines and air pockets. In addition, the simulation of the phase transition to calculate shrinkage and warpage would be an important step towards a fully functional mesh-free injection molding tool.

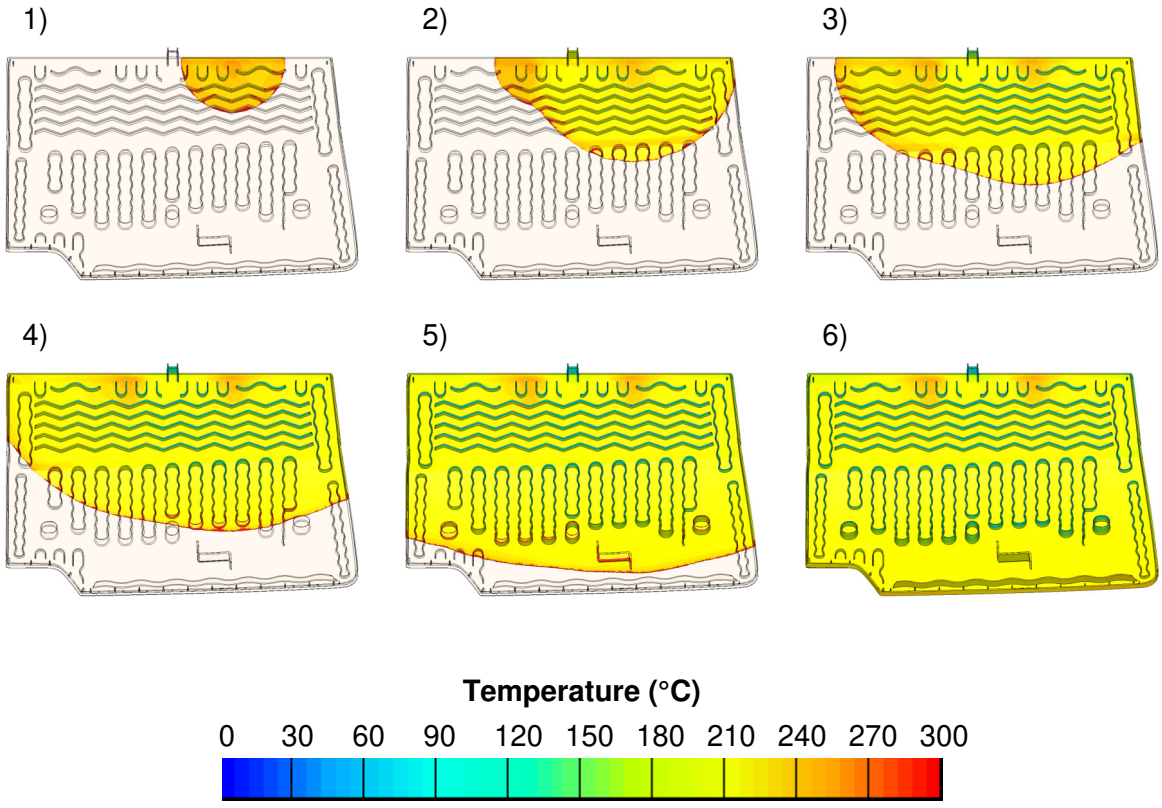

FIG. 14. Filling pattern of injection molding process for glove box door using commercial code CADMOULD

ACKNOWLEDGEMENTS

Raw material for the experiments, and the corresponding material data for this study was provided by LyondellBasell.

Pratik Suchde would like to acknowledge partial support from the European Union's Horizon 2020 research and innovation programme under the Marie Skłodowska-Curie Actions grant agreement No. 892761 "SURFING".

DATA AVAILABILITY STATEMENT

The data that support the findings of this study are available from the corresponding author upon reasonable request.

Appendix A: Material Parameters

The material parameters used in section VI for PPGF25 and PPGF30 are presented in tables IV - IX. While the viscosity and density are modelled by analytical functions, the heat capacity and thermal conductivity are given as tables depending on the temperature.

TABLE IV. *2-Domain-Tait* Parameters

Parameter	**PPGF25**	**PPGF30**
b_1^s $(\frac{m^3}{kg})$	0.000979	0.0009159
b_1^m $(\frac{m^3}{kg})$	0.00103	0.001003
b_2^s $(\frac{m^3}{kg \cdot K})$	4.93E-7	3.28E-7
b_2^m $(\frac{m^3}{kg \cdot K})$	6.76E-7	7.678E-7
b_3^s (Pa)	1.46E8	2.177553E8
b_3^m (Pa)	9.83E7	1.03095E8
b_4^s $(\frac{1}{K})$	0.00509	0.00437
b_4^m $(\frac{1}{K})$	0.005	0.006285
b_5 (K)	430.0	433.15
b_6 $(\frac{K}{Pa})$	8.5E-8	1.105E-7
b_7 $(\frac{m^3}{kg})$	5.1E-5	8.722E-5
b_8 $(\frac{1}{K})$	0.156	0.1242
b_9 $(\frac{1}{Pa})$	1.84E-8	1.746E-8

TABLE V. *Cross-WLF* Parameters

Parameter	**PPGF25**	**PPGF30**
A_1 (-)	26.264	32.271
A_2 (K)	51.6	51.6
D_1 $(Pa \cdot s)$	1.5E12	2.5E14
D_2 (K)	263.15	263.15
n (-)	0.4069	0.345
τ^* (Pa)	11204.9	17000.5

TABLE VI. PPGF25 heat capacity c_v

Temperature $(^\circ C)$	$\mathbf{c}_v$ $(\frac{J}{kg \cdot K})$
111.79	2025.3
115.97	2263.1
120.33	3260.8
122.59	4702.3
125.65	6810.8
128.33	3396.0
130.31	2128.2
131.33	1977.2
132.36	1925.9
172.57	2013.0
222.09	2116.6
244.77	2163.8
251.96	2153.7

TABLE VII. PPGF30 heat capacity c_v

Temperature $(^\circ C)$	$\mathbf{c}_v$ $(\frac{J}{kg \cdot K})$
45.0	1218.0
80.0	1438.0
108.0	1723.0
118.0	2136.0
121.0	3080.0
124.0	17153.0
125.0	17153.0
129.0	2290.0
131.0	1720.0
180.0	1791.0
250.0	1918.0

TABLE VIII. PPGF25 thermal conductivity λ

Temperature $(^\circ C)$	λ $(\frac{W}{m \cdot K})$
65.0	0.320
80.0	0.323
100.0	0.325
120.0	0.322
140.0	0.313
160.0	0.242
180.0	0.238
200.0	0.235
220.0	0.232
240.0	0.230
250.0	0.228

TABLE IX. PPGF30 thermal conductivity λ

Temperature $(^{\circ}C)$	λ $(\frac{W}{m \cdot K})$
31.9	0.234
48.7	0.232
68.5	0.23
88.2	0.2223
108.6	0.225
128.4	0.227
144.0	0.206
160.6	0.191
181.2	0.193
200.6	0.193
217.6	0.193
235.5	0.194

REFERENCES

[1]C. Fernandes, A. J. Pontes, J. C. Viana, and A. Gaspar-Cunha, "Modeling and optimization of the injection-molding process: A review," Adv. Polym. Technol. **37**, 429–449 (2018), DOI:10.1002/adv.21683.

[2]C. A. Hieber and S. F. Shen, "A finite-element/finite-difference simulation of the injection-molding filling process," J. Non-newtonian Fluid Mech. **7**, 1–32 (1980), DOI:10.1016/0377-0257(80)85012-9.

[3]M. Ren, J. Gu, Z. Li, S. Ruan, and C. Shen, "Simulation of polymer melt injection molding filling flow based on an improved sph method with modified low-dissipation riemann solver," Macromol. Theory and Simul. **31**, 2100029 (2022), DOI:10.1002/mats.202100029.

[4]C. Shen, W. Lixia, and Q. Li, "Optimization of injection molding process parameters using combination of artificial neural network and genetic algorithm method," J. Mater. Process. Technol. **183**, 412–418 (2007), DOI:10.1016/j.jmatprotec.2006.10.036.

[5]M. V. Bruschke and S. G. Advani, "A finite element/control volume approach to mold filling in anisotropic porous media," Polym. Compos. **11**, 398–405 (1990), DOI:10.1002/pc.750110613.

[6]E. Holm and H. P. Langtangen, "A unified finite element model for the injection molding process," Comput. Methods Appl. Mech. Eng. **178**, pp.413–429, (1999), DOI:10.1016/S0045-7825(99)00029-8.

[7]H. Chen, P. Wapperom, and D. G. Baird, "The use of flow type dependent strain reduction factor to improve fiber orientation predictions for an injection molded center-gated disk," Phys. Fluids **31**, 123105 (2019), DOI:10.1063/1.5129679.

[8]R.-Y. Chang and W.-h. Yang, "Numerical simulation of mold filling in injection molding using a three-dimensional finite volume approach," Int. J. Numer. Methods Fluids **37**, 125–148 (2001), DOI:10.1002/fld.166.

[9]P. H. Foss, H.-C. Tseng, J. Snawerdt, Y.-J. Chang, W.-h. Yang, and C.-H. Hsu, "Prediction of fiber orientation distribution in injection molded parts using moldex3d simulation," Polym. Compos. **35**, 671–680 (2014), DOI:10.1002/pc.22710.

[10]S. Xue, N. Phan-Thien, and R. I. Tanner, "Three dimensional numerical simulations of viscoelastic flows through planar contractions," J. Non-Newtonian Fluid Mech. **74**, 195–245 (1998), DOI:10.1016/S0377-0257(97)00072-4.

[11]E. Bertevas, J. Férec, B. C. Khoo, G. Ausias, and N. Phan-Thien, "Smoothed particle hydrodynamics (sph) modeling of fiber orientation in a 3d printing process," Phys. Fluids **30**, 103103 (2018), DOI:10.1063/1.5047088.

[12]Y. Morii and T. Kawakatsu, "Lagrangian multiscale simulation of complex flows," Phys. Fluids **33**, 093106 (2021), DOI:10.1063/5.0063059.

[13]T. Ye, D. Pan, C. Huang, and M. Liu, "Smoothed particle hydrodynamics (sph) for complex fluid flows: Recent developments in methodology and applications," Phys. Fluids **31**, 011301 (2019), DOI:10.1063/1.5068697.

[14]X.-J. Fan, R. I. Tanner, and R. Zheng, "Smoothed particle hydrodynamics simulation of non-newtonian moulding flow," J. Non-Newtonian Fluid Mech. **165**, 219–226 (2010), DOI:10.1016/j.jnnfm.2009.12.004.

[15]L. He, G. Lu, D. Chen, W. Li, L. Chen, J. Yuan, and C. Lu, "Smoothed particle hydrodynamics simulation for injection molding flow of short fiber-reinforced polymer composites," J. Compos. Mater. **52**, 1531–1539 (2017), DOI:0.1177/0021998317726365.

[16]K. Wu, L. Wan, H. Zhang, and D. Yang, "Numerical simulation of the injection molding process of short fiber composites by an integrated particle approach," The International Journal of Advanced Manufacturing Technology **97**, 3479–3491 (2018).

[17]X. Xu and P. Yu, "Modeling and simulation of injection molding process of polymer melt by a robust sph method," Appl. Math. Modell. **48**, 384–409 (2017), DOI:10.1016/j.apm.2017.04.007.

[18]X. Xu and P. Yu, "Extension of sph to simulate non-isothermal free surface flows during the injection molding process," Appl. Math. Modell. **73**, 715–731 (2019), DOI:10.1016/j.apm.2019.02.048.

[19]J. Kuhnert, *General smoothed particle hydrodynamics*, Ph.D. thesis, Technische Universität Kaiserslautern, Aachen (1999).

[20]A. Jefferies, J. Kuhnert, L. Aschenbrenner, and U. Giffhorn, "Finite pointset method for the simulation of a vehicle travelling through a body of water," in *Meshfree Methods for Partial Differential Equations VII*, edited by M. Griebel and M. A. Schweitzer (Springer International Publishing, Cham, 2015) pp. 205–221.

[21]I. Michel, S. M. I. Bathaeian, J. Kuhnert, D. Kolymbas, C.-H. Chen, I. Polymerou, C. Vrettos, and A. Becker, "Meshfree generalized finite difference methods in soil mechanics—part ii: numerical results," GEM Int. J. Geomath. **8**, 191–217 (2017), DOI:10.1007/s13137-017-0096-5.

[22]I. Michel, T. Seifarth, J. Kuhnert, and P. Suchde, "A meshfree generalized finite difference method for solution mining processes," Comput. Part. Mech. **8**, 561–574 (2020), DOI:10.1007/s40571-020-00353-2.

[23]E. O. Reséndiz-Flores, J. Kuhnert, and F. R. Saucedo-Zendejo, "Application of a generalized finite difference method to mould filling process," European Journal of Applied Mathematics **29**, 450–469 (2018).

[24]E. Oñate, J. Rojek, M. Chiumenti, S. Idelsohn, F. Del Pin, and R. Aubry, "Advances in stabilized finite element and particle methods for bulk forming processes," Comput. Methods Appl. Mech. Eng. **195**, 6750–6777 (2006), computational Metal Forming, DOI:10.1016/j.cma.2004.10.018.

[25]K. Butler, E. Oñate, S. Idelsohn, and R. Rossi, "Modeling polymer melt flow using the particle finite element method (pfem)," Proceeding of the Interflam Conference 2007 **2** (2007).

[26]M. Cremonesi, A. Franci, S. Idelsohn, and E. Oñate, "A state of the art review of the particle finite element method (pfem)," Arch. Comput. Methods Eng. **27**, 1709–1735 (2020), DOI:10.1007/s11831-020-09468-4.

[27]Grand View Research, "Injection molded plastics market size, share & trends analysis report by raw material (polypropylene, abs, hdpe, polystyrene), by application (packaging, automotive & transportation, medical), by region, and segment forecasts, 2021 - 2028," (2021).

[28]D. V. Rosato, D. V. Rosato, and M. G. Rosato, eds., *Injection Molding Handbook*, third edition ed., Springer eBook Collection (Springer US, Boston, MA, 2000) DOI:10.1007/978-1-4615-4597-2.

[29]R. Zheng, R. I. Tanner, and X. J. Fan, *Injection Molding: Integration of Theory and Modeling Methods* (Springer Berlin Heidelberg, 2011).

[30]H. Zhou, ed., *Computer modeling for injection molding: Simulation, optimization, and control* (Wiley, Hoboken, N.J., 2013).

[31]D. W. van Krevelen and K. t. Nijenhuis, *Properties of polymers: Their correlation with chemical structure ; their numerical estimation and prediction from additive group contributions*, 4th ed. (Elsevier, Amsterdam, 2009).

[32]P. Zoller and Y. A. Fakhreddine, "Pressure-volume-temperature studies of semi-crystalline polymers," Thermochim. Acta **238**, 397–415 (1994), DOI:10.1016/S0040-6031(94)85221-9.

[33]C. A. Hieber, "Modelling the pvt behavior of isotactic polypropylene," Int. Polym. Proc. **12**, 249–256 (1997), DOI:10.3139/217.970249.

[34]N. Rudolph and T. A. Osswald, *Polymer Rheology: Fundamentals and Applications* (Carl Hanser Verlag GmbH & Company KG, 2014).

[35]P. Suchde, J. Kuhnert, S. Schröder, and A. Klar, "A flux conserving meshfree method for conservation laws," Int. J. Numer. Methods Eng. **112**, 238–256 (2017), DOI:10.1002/nme.5511.

[36]R. Brunotte, *Die thermodynamischen und verfahrenstechnischen Abläufe der in-situ-Oberflächenmodifizierung beim Spritzgießen*, Schriftenreihe Kunststoffe (FKTU, 2006).

[37]P. Suchde and J. Kuhnert, "Point cloud movement for fully lagrangian meshfree methods," J. Comput. Appl. Math. **340**, 89 – 100 (2018), DOI:10.1016/j.cam.2018.02.020.

[38]H. A. van der Vorst, "Bi-cgstab: A fast and smoothly converging variant of bi-cg for the solution of nonsymmetric linear systems," SIAM J.Scient. Statistic. Comput. **13**, 631–644 (1992), DOI:10.1137/0913035.

[39]P. Suchde, J. Kuhnert, and S. Tiwari, "On meshfree GFDM solvers for the incompressible Navier–Stokes equations," Comput. Fluids **165**, 1 – 12 (2018), DOI:10.1016/j.compfluid.2018.01.008.

[40]J. Kuhnert, "Meshfree numerical scheme for time dependent problems in fluid and continuum mechanics," in *Advances in PDE Modeling and Computation*, edited by S. Sundar (Anne Books, New Delhi, 2014) pp. 119–136.

[41]C. Drumm, S. Tiwari, J. Kuhnert, and H.-J. Bart, "Finite pointset method for simulation of the liquid - liquid flow field in an extractor," Comput. Chemic. Engin. **32**, 2946 – 2957 (2008), DOI:10.1016/j.compchemeng.2008.03.009.

[42]B. Seibold, *M-Matrices in Meshless Finite Difference Methods*, Ph.D. thesis, Kaiserslautern University (2006).

[43]T. Seifarth, *Numerische Algortihmen für gitterfreie Methoden zur Lösung von Transportproblemen*, Ph.D. thesis, University of Kassel, Kassel (2017).

[44]E. Kwan-yu Chiu, Q. Wang, R. Hu, and A. Jameson, "A conservative mesh-free scheme and generalized framework for conservation laws," SIAM J. Scient. Comput. **34**, 2896–2916 (2012), DOI:10.1137/110842740.

[45]P. Suchde, *Conservation and Accuracy in Meshfree Generalized Finite Difference Methods*, Ph.D. thesis, University of Kaiserslautern, Kaiserslautern, Germany (2018).

[46]T. Liszka and J. Orkisz, "Special issue-computational methods in nonlinear mechanics the finite difference method at arbitrary irregular grids and its application in applied mechanics," Comput. Struct. **11**, 83–95 (1980), DOI:10.1016/0045-7949(80)90149-2.

[47]J. Benito, F. Ureña, and L. Gavete, "Influence of several factors in the generalized finite difference method," Appl. Math. Modell. **25**, 1039–1053 (2001), DOI:10.1016/S0307-904X(01)00029-4.

[48]S. Milewski, "Selected computational aspects of the meshless finite difference method," Numerical Algorithms **63**, 107–126 (2013), DOI:10.1007/s11075-012-9614-6.

[49]C.-M. Fan, C.-N. Chu, B. Šarler, and T.-H. Li, "Numerical solutions of waves-current interactions by generalized finite difference method," Eng. Anal. Boundary Elem. **100**, 150–163 (2019), DOI:10.1016/J.ENGANABOUND.2018.01.010.

[50]P. Suchde, "A meshfree lagrangian method for flow on manifolds," Int. J. Numer. Methods Fluids **93**, 1871–1894 (2021), DOI:10.1002/fld.4957.

[51]Y. Wang, Y. Gu, and J. Liu, "A domain-decomposition generalized finite difference method for stress analysis in three-dimensional composite materials," Appl. Math. Lett. **104**, 106226 (2020), DOI:10.1016/j.aml.2020.106226.

[52]H. Xia and Y. Gu, "Generalized finite difference method for electroelastic analysis of three-dimensional piezoelectric structures," Appl. Math. Lett. **117**, 107084 (2021), DOI:10.1016/j.aml.2021.107084.

[53]J. P. Morris, P. J. Fox, and Y. Zhu, "Modeling low reynolds number incompressible flows using sph," J. Comput. Phys. **136**, 214–226 (1997), DOI:10.1006/jcph.1997.5776.

[54]J. O. Cruickshank, "Low-reynolds-number instabilities in stagnating jet flows," J. Fluid Mech. **193**, 111–127 (1988), DOI:10.1017/S0022112088002071.

[55]E. Mitsoulis, "Fountain flow of pseudoplastic and viscoplastic fluids," J. Non-Newtonian Fluid Mech. **165**, 45–55 (2010), DOI:10.1016/j.jnnfm.2009.09.001.

[56]X.J. Fan, R.I. Tanner, and R. Zheng, "Smoothed particle hydrodynamics and its application to non-newtonian moulding flow," in *Injection Molding: Process, Design, and Applications*, edited by Phoebe H. Kauffer (Nova Science Publishers, 2011) pp. 101–154.